Materials Today Bio 35 (2025) 102508

Contents lists available at ScienceDirect

Materials Today Bio

journal homepage: www.journals.elsevier.com/materials-today-bio

Thermo-responsive shape memory biomaterials with structural and physical adaptivity for scarless personalized nerve repair

Tao Gao [a,1], Jiahui Song [b,1], Lu Li [c,1], Junqing Lin [a], Junjie Shen [a], Yun Qian [a,2,*], Xiumei Mo [b,2,**], Xianyou Zheng [a,2,***]

[a] *National Center for Orthopaedics, Department of Orthopaedics, Shanghai Sixth People's Hospital Affiliated to Shanghai Jiao Tong University School of Medicine, Shanghai, 200233, China*
[b] *State Key Laboratory for Modification of Chemical Fibers and Polymer Materials, Shanghai Engineering Research Center of Nano-Biomaterials and Regenerative Medicine, College of Biological Science and Medical Engineering, Donghua University, Shanghai, 201620, China*
[c] *Department of Plastic Surgery, Naval Medical Center, (Naval Medical University), Shanghai, 200052, China*

ARTICLE INFO

Keywords:
Shape memory
Nerve repair
Biomaterials
Multichannel
Personalized

ABSTRACT

Nerve guidance conduits (NGCs) have emerged as promising alternatives to autologous nerve grafts for peripheral nerve repair, overcoming donor site morbidity while promoting axonal regeneration. However, size and structure mismatch in conventional NGCs impairs axon sprouting, remyelination and neural regeneration efficacy. Here, we engineered a thermo-responsive self-rolling multichannel NGC comprising shape-memory poly (lactide-co-trimethylene carbonate) (PLMC), silk fibroin (SF), and reduced graphene oxide (rGO) to enable scarless regeneration with personalized anatomical matching. The electrospun PLMC/SF-rGO conduit features axially aligned inner fibers providing topographical guidance cues for directional guidance and exhibits programmable shape recovery, enabling intraoperative customization and shape resistance throughout the nerve regeneration period. In vitro, 0.5 % rGO optimally enhanced Schwann cell migration, proliferation and neuronal proliferation. In vivo assessment in rat 10-mm sciatic defects over 12 weeks demonstrated that PLMC/SF-rGO NGCs significantly outperformed PLMC/SF controls in functional recovery, reduced muscle atrophy, and decreased fibrosis. Histology further confirmed superior axonal regeneration and marker expression (NF200/S100β), achieving outcomes comparable to autografts. This multichannel NGC synergizes structural and physical adaptability, electrical conductivity, and bioactive cues to accelerate nerve regeneration, offering a promising alternative to autografts for scarless personalized repair.

1. Introduction

Peripheral nerve injury (PNI), a prevalent disorder affecting the nervous system, arises from diverse etiologies including trauma, surgical complications, congenital anomalies, and combat-related wounds [1]. PNI results in persistent sensorimotor deficits, imposing significant socioeconomic burdens and substantially diminishing patients' quality of life [2]. Although the peripheral nervous system (PNS) exhibits greater regenerative capacity than the central nervous system (CNS), clinical outcomes following PNI remain suboptimal due to the inherently slow and incomplete nature of neuronal regeneration [3,4]. Autologous nerve transplantation represents the current gold standard

---

This article is part of a special issue entitled: Multiscale Composites published in Materials Today Bio.

[*] Corresponding author. Department of Orthopaedic Surgery, Shanghai Sixth People's Hospital Affiliated to Shanghai Jiao Tong University School of Medicine, No. 600, Yishan Road, Xuhui District, Shanghai, China.

[**] Corresponding author. Department of Orthopaedic Surgery, Shanghai Sixth People's Hospital Affiliated to Shanghai Jiao Tong University School of Medicine, No. 600, Yishan Road, Xuhui District, Shanghai, China.

[***] Corresponding author. State Key Laboratory for Modification of Chemical Fibers and Polymer Materials, Shanghai Engineering Research Center of Nano-Biomaterials and Regenerative Medicine, College of Biological Science and Medical Engineering, Donghua University, No. 2999, Renmin North Road, Songjiang District, Shanghai, China.

E-mail addresses: sakio@sjtu.edu.cn (Y. Qian), xmm@dhu.edu.cn (X. Mo), zhengxianyou@126.com (X. Zheng).

[1] These authors contributed equally and shared co-first authors.

[2] These authors contributed equally and shared co-senior authors.

https://doi.org/10.1016/j.mtbio.2025.102508
Received 10 October 2025; Received in revised form 31 October 2025; Accepted 1 November 2025
Available online 3 November 2025
2590-0064/© 2025 The Authors. Published by Elsevier Ltd. This is an open access article under the CC BY-NC-ND license (http://creativecommons.org/licenses/by-nc-nd/4.0/).

for treating critical-sized peripheral nerve defects [5]; however, its utility is constrained by unavoidable donor site morbidity, including persistent abnormal sensation, numbness, and even neuropathic pain [6–11].

Over recent decades, nerve guidance conduits (NGCs) have emerged as promising alternatives, designed to guide axonal regeneration through tailored physical and chemical cues while promoting Schwann cell proliferation and differentiation [12–17]. A significant limitation of clinically available NGCs is their restricted dimensional range, which impedes precise matching to peripheral nerve defect size and structure [18]. Oversized conduits compromise guidance efficiency and promote fibrotic tissue proliferation, whereas undersized conduits induce kinking and ischemic compression, ultimately impairing neural regeneration efficacy [19], as shown in Fig. 1.

Shape-memory polymer-based nerve guidance conduits (SMP-NGCs) achieve dimensional compatibility with neural tissues via thermo-responsive phase transitions [20,21]. These conduits generate programmable radial expansion forces through entropy-driven molecular chain reorganization, counteracting perineurial pressure gradients to stabilize the endoneurial microenvironment during the Wallerian degeneration phase (weeks 1–4 post-implantation) [22]. The biodegradable copolymer poly(lactide-co-trimethylene carbonate) (PLMC), synthesized from FDA-approved polylactic acid (PLA) and polytrimethylene carbonate (PTMC), serves as a key material type for SMP-NGCs [23–26]. PLMC demonstrates excellent biocompatibility, evidenced by minimal inflammatory response and favorable cellular interactions, facilitating its application in osteosynthesis devices, vascular stents, and tissue-engineered nanofiber membranes [27–29].

To address PLMC's limited capacity for supporting neuronal growth, we integrated silk fibroin (SF), a natural biopolymer derived from Bombyx mori cocoons through controlled degumming. SF exhibits high mechanical properties, exceptional biocompatibility, tunable degradability, and broad utility in tissue engineering, drug delivery, and regenerative medicine [30,31].

Electrical conductivity represents a critical characteristic for NGCs, as conductive materials facilitate bioactive signaling to enhance axonal extension [32]. Various conductive biomaterials—including polyaniline (PANi), poly(3,4-ethylenedioxythiophene) (PEDOT), polypyrrole (PPy), graphene, and their derivatives—have been employed in NGC fabrication [33,34]. Graphene, in particular, offers exceptional electrical conductivity, mechanical strength, tunable topography, and large surface area [35]. However, its biomedical application is constrained by inherent hydrophobicity, poor aqueous dispersibility, and dose-dependent cytotoxicity [36]. Graphene oxide (GO), an oxidized derivative, exhibits superior aqueous dispersibility due to oxygen-containing functional groups and enhanced processability compared to pristine graphene [37,38]. Crucially, GO can be reduced in situ to restore electrical conductivity while maintaining improved biocompatibility [39].

In this study, we fabricate a three-channel NGC composed of PLMC, SF, and GO via electrospinning, subsequently reduced in situ to PLMC/SF-rGO using L-ascorbic acid (Fig. 2). Electrospun aligned fibers promote directional nerve cell outgrowth through oriented topological cues [40]. The biomimetic multichannel design recapitulates the hierarchical architecture of native peripheral nerve, a strategy widely incorporated into advanced NGCs [41,42]. We evaluate biocompatibility, proliferation, adhesion, and neural differentiation using rat Schwann cells (RSC96) and PC12 cells—established models for peripheral nerve regeneration studies. Functional and histological analyses confirm that the conductive PLMC/SF-rGO NGC significantly enhances nerve

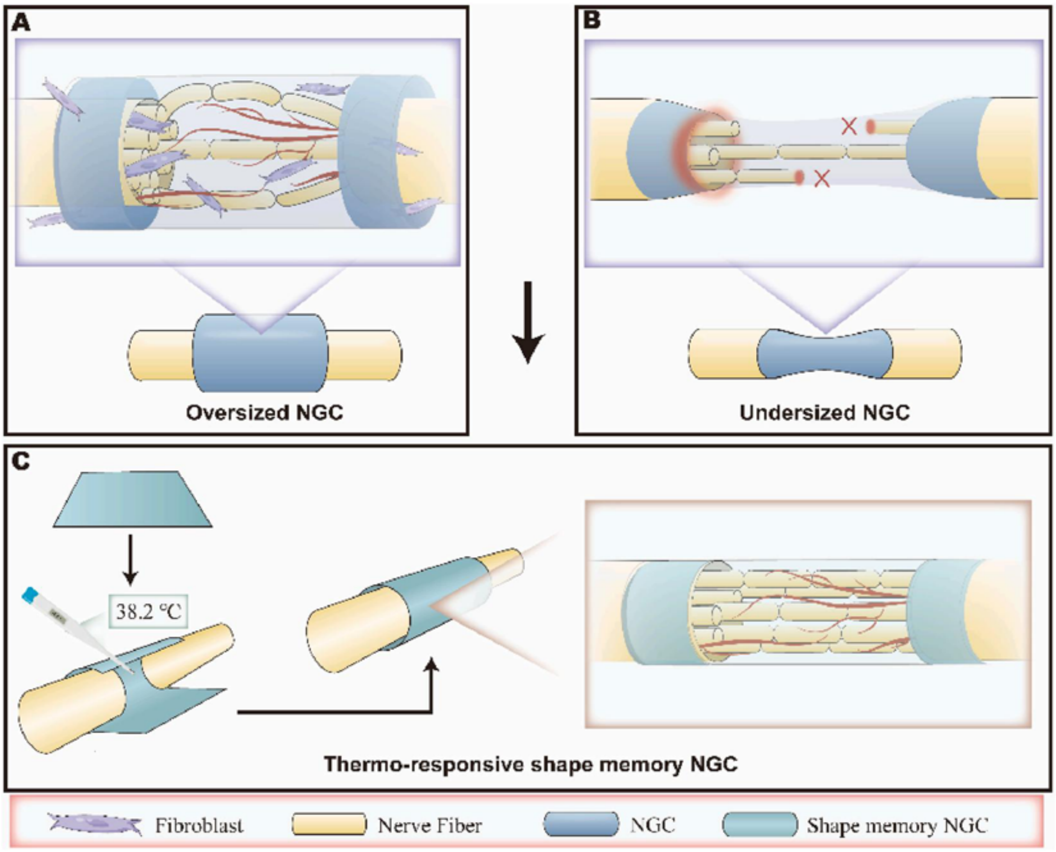

Fig. 1. Thermo-responsive shape memory in peripheral nerve defect repair. (A) Oversized NGC compromise guidance efficiency and promote fibrotic tissue proliferation. (B) Undersized NGC induce kinking and ischemic compression. (C) Thermo-responsive shape memory NGC undergoes autonomous curling to circumferentially encapsulate the nerve, enabling tension-free coaptation with optimal anatomical alignment.

Fig. 2. Schematic illustration of the three-channel PLMC/SF-rGO NGCs and its application in repairing sciatic nerve defects in rats.

regeneration, evidenced by improvements in sciatic functional index (SFI), electromyography (EMG) recordings, and muscle weight ratio. Collectively, these results demonstrate that our PLMC/SF-rGO NGC effectively accelerates functional recovery and axonal regeneration in rat models with critical-length sciatic nerve defects. This nerve conduit system establishes a technical framework for personalized clinical management of peripheral nerve defects, enabling tension-free repair with minimal scarring.

2. Materials and methods

2.1. Materials

Poly (lactide-co-trimethylene carbonate, PLMC, LA: TMC = 7:3) was provided by Jinan Daigang Co., Ltd. (Jinan, China). 1,1,1,3,3,3-Hexafluoro-2-propanol (HFIP, 920-66-1) was obtained from Shanghai Darui Fine Chemical Co., Ltd. (Shanghai, China). Graphene oxide (GO, 1034343-98-0) was purchased from Macklin Co., Ltd. (Shanghai, China). L-Ascorbic acid (50-81-7) was purchased from China National Pharmaceutical Group (Shanghai, China). Silkworm cocoons (Bombyx mori) was from the Sericulture Base of Northwest China (Shanxi, China). Schwann 96 cells (RSC96) and PC12 cells were provided by the Institute of Biochemistry and Cell Biology (Shanghai, China).

2.2. Extraction of silk fibroin (SF)

Silkworm cocoons (60 g) were degummed by boiling in 0.5 M Na_2CO_3 solution (30 g in 1 L deionized water) for 30 min, repeated three times. Dried cocoons were dissolved in 9 M LiBr solution with stirring until complete dissolution. The solution was dialyzed (3 days, distilled water) to remove salts, followed by filtration and lyophilization to obtain purified SF.

2.3. Fabrication and characterization of NGCs

2.3.1. Fabrication of nanofiber membranes

As reported in previous work, the Tg of PLMC increases with higher LA content due to the enhanced chain rigidity of the lactide units. The 7:3 LA:TMC ratio provides a Tg of approximately 37 °C, which makes it ideal for this thermally triggered shape-memory behavior [43]. PLMC was dissolved in HFIP to prepare a 12 % (w/v) electrospinning solution. For PLMC/SF solutions, PLMC and SF (9:1 w/w) were dissolved in HFIP to achieve 12 % concentration. Sonicated GO nanoparticles (0.25–2 wt% relative to polymer mass) were dispersed in PLMC or PLMC/SF solutions. Membranes were electrospun (SS-3556H, Yongkang Leye Technology, China) under standardized parameters: flow rate 1 mL/h, 20G needle, voltage 14 kV, collector speed 3000 rpm (aligned fibers) or 200 rpm (random fibers), with ambient humidity maintained at 40 % and temperature at 25 °C. PLMC-GO and PLMC/SF-GO membranes were reduced to PLMC-rGO and PLMC/SF-rGO by immersion in L-ascorbic acid for 48 h at room temperature. All membranes were vacuum-dried overnight.

2.3.2. Multichannel NGC Assembly

To prepare the PLMC, PLMC-rGO, PLMC/SF and PLMC/SF-rGO NGCs, membranes were cut to dimensions of 10 mm × 20 mm and wrapped around steel rods, ensuring that the aligned layer was in direct contact with the rod and that the nanofibers were oriented along its longitudinal axis. Then, the assemblies were subjected to thermal treatment at 60 °C for 30 min in an oven to facilitate the formation of tubular structures. Steel rods of different diameters templated tubes with inner diameters of 0.8 mm and 2 mm. The tubes were temporarily flattened into planar configurations at 0 °C under external pressure. For the smaller tubes (0.8 mm diameter), their original tubular shapes were restored by immersion in distilled water at 40 °C. In a subsequent step, three such small parallel tubes were positioned on a larger membrane at 0 °C. Upon heating to 40 °C, both the large membrane and the small tubes underwent shape recovery, leading to the large membrane enveloping the three smaller tubes to form the multichannel NGCs.

2.3.3. Characterization of NGCs

The morphologies of the PLMC, PLMC-rGO, PLMC/SF, and PLMC/SF-rGO nanofibers were identified by scanning electron microscopy (SEM, Hitachi TM-1000, Japan) after sputter coating with gold. At least 100 nanofibers randomly selected from each sample were measured for average diameter and angle distribution of aligned nanofibers by Image J software (National Institutes of Health, v1.8.0, USA). The mechanical properties of these membranes (10 mm × 30 mm, n = 6) were measured using a material testing machine (HY-940FS, China).

The thermal properties of PLMC, PLMC-rGO, PLMC/SF, and PLMC/SF-rGO membranes were evaluated using differential scanning calorimetry (DSC) on a TA instrument (204 F1 Netzsch, Germany), following a previously established method [43]. To verify the loading and reduction of GO, Fourier transform infrared spectroscopy (FTIR, Nicolet Instrument, Madison, USA) was utilized for characterization of these membranes.

The conductivity of membranes was measured in wet state using a digital multimeter (8901S, Chenzhou Island Industrial Co., Ltd, Shenzhen, China). The cross-sectional area (A) was determined from width and thickness measurements using vernier calipers, and Conductivity (σ) was calculated as: $\sigma = \frac{L}{AR}$.where, R represented the membrane resistance (MΩ); L was the inter-electrode distance (cm); and A was the cross-sectional area (cm^2).

To assess the in vitro degradation profile and structural stability of the NGCs, each sample was immersed in 2 mL of PBS and incubated at 37 °C under continuous shaking at 100 rpm for 30 days. Following this period, the conduits were rinsed with deionized water, freeze-dried, and subsequently analyzed to determine the extent of degradation.

2.4. Cell culture and proliferation assay

RSC96 and PC12 cells were cultured in high-glucose DMEM supplemented with 10 % FBS and 1 % penicillin/streptomycin at 37 °C/5 % CO_2. Nanofiber membranes were sterilized in ethanol (4 h) followed by UV exposure overnight.

2.4.1. Cytotoxicity and proliferation (CCK-8)

Cells (2×10^4 cells/cm^2) were seeded on membranes. Optimal rGO concentration was determined using PLMC/SF membranes with 0–2 % rGO after 24 h culture. CCK-8 solution (20 μL) was added to 200 μL medium/well; after 4 h incubation, absorbance (450 nm) was measured (Thermo 3001 reader, USA). The serum-free medium served as the negative control, while serum-free medium supplemented with 10 % DMSO was used as the positive control. Six independent samples were evaluated with RSC96 cells for each nanofiber membrane. Then, CCK8 assay was also used to assess the RSC96 or PC12 cell proliferation after seeded on the PLMC, PLMC-rGO, PLMC/SF or PLMC/SF-0.5 %rGO nanofiber membranes for 1, 4 and 7 days.

2.4.2. Cell viability assay

RSC96 or PC12 cells cultured on PLMC, PLMC-rGO, PLMC/SF or PLMC/SF-0.5 %rGO nanofiber membranes were stained after 24 h (LIVE/DEAD kit, Invitrogen) and imaged by phase-contrast microscopy. Relative cell viability, defined as the percentage of viable cells, was assessed using ImageJ software (n = 5).

2.4.3. Cell morphology and differentiation

To observe the cell morphology, F-actin was stained after 4 days of culture on PLMC, PLMC-rGO, PLMC/SF or PLMC/SF-0.5 %rGO nanoscaffold membranes. Cells were washed with PBS (3 ×), fixed in 4 % paraformaldehyde (30 min), and permeabilized in 0.1 % Triton X-100 (Sigma; 5 min). Actin filaments were stained with Phalloidin (1:1000, Yeasen), and nuclei with DAPI (1:500, Gibco). Samples were imaged by inverted fluorescence microscopy. Relative inflorescence intensity of Phalloidin per cell, percentage of differentiated PC12 cells and the neurite length were measured by ImageJ software (n = 5).

2.4.4. Cell adhesion

PC12 cells were cultured on PLMC, PLMC-rGO, PLMC/SF or PLMC/SF-0.5 %rGO nanoscaffold membranes for 4 d. The medium was replaced every 2 d. The adhesion of the PC12 cells on the different nanofiber membranes was observed by SEM. First, the medium was removed from the cell culture and replaced with fresh Dulbecco's PBS (Gibco, USA). Cells on nanofiber membranes were fixed with 2.5 % glutaraldehyde (12 h, 4 °C). After fixation, samples were treated with 1 % osmium tetroxide (2 h, 4 °C), then dehydrated through a graded ethanol series (30 %, 50 %, 70 %, 80 %, 90 %, 95 %, 100 %) with two 20-min incubations per concentration. Following lyophilization and gold sputter-coating, cell adhesion was evaluated by SEM.

2.4.5. Migration

Transwell migration assay: Transwell inserts with polycarbonate membranes (pore size, 8.0 μm, Coring, USA) were placed into 24-well plates and incubated with 1 mL of serum-free medium and 200 μL of extraction solution (n = 6). And upper chamber of each insert received 200 μL cell suspension (2×10^4 cells/mL). After 24 h, inserts were rinsed with PBS, and cells were stained with 500 μL of crystal violet solution (Sigma Aldrich Corp., St. Louis, Missouri, USA) for 15 min, after fixed with 500 μL of 4 % paraformaldehyde (PFA). Non-migrated cells on the upper membrane surface were removed with a cotton swab, and migrated cells were then imaged by light microscopy. The inserts were then transferred to new 24-well plates, and the crystal violet stain was extracted using 10 % (v/v) acetic acid. The OD values of each sample were measured at 590 nm after transferring the solution to a 96-well plate. The migration rates of RSC96 cells were calculated from OD values.

Scratch assay: RSC96 cells (5×10^4 cells/well) were cultured in 24-well plates in 1 mL DMEM complete medium. Upon reaching confluence as a monolayer after 24 h of culture, a scratch assay was performed. Using a 100 μL pipette tip aligned vertically with the aid of a ruler, three parallel scratches were made in each well, ensuring consistent spacing. The scratched wells were gently rinsed several times with PBS to remove floating cells. The culture medium was replaced with 1 mL of serum-free medium as control group. The experimental group received 1 mL of extract prepared by incubating 100 mg of graft material in 5 mL of serum-free medium at 37 °C for 24 h. The plates were then returned to the incubator. Images were captured immediately after treatment (0 h) and again at 24 h under a microscope. The scratch healing area was measured by Image J software (n = 5). The area recovery was calculated by the following equation: ((average gap distance (0 h) – average gap distance at (24 h))/average gap distance (0 h) *100 %.

2.5. Animal surgery and evaluation

All procedures were approved by Shanghai Chengxi Biotechnology Co., Ltd (Approval No.: CX052404066). Based on the in vitro screening results, the optimal rGO concentration (0.5 wt%) was used for the fabrication of PLMC/SF-rGO conduits for all in vivo studies. Thirty male Sprague-Dawley rats (150–200 g) were acclimatized (SPF facility, 1 week) and randomly assigned (n = 10/group): autograft, PLMC/SF conduit, and PLMC/SF-rGO conduit. Under pentobarbital anesthesia (40 mg/kg, i.p.), a 10-mm segment of the sciatic nerve was excised from the right hindlimb to create a critical-sized defect [44]. In the conduit groups, the defect was bridged using the appropriate nerve guide conduit, secured with 6-0 nylon epineurial sutures. In the autograft group, the removed 10-mm nerve segment was flipped 180° and reinserted to bridge the defect. Muscle and skin were closed (3-0 nylon). Postoperative penicillin (800,000 IU, i.m.) was administered. Outcomes were assessed at 6 and 12 weeks. The 6-week time point represents a mid-stage phase of nerve regeneration when initial reinnervation occurs, while the 12-week time point corresponds to a more advanced recovery phase, allowing assessment of mature axonal and functional restoration.

2.5.1. Functional evaluation

Each group was evaluated for infection, edema, and surgical wound healing status. The recovery of sciatic nerve function was assessed using walking tracks and electrophysiological analyses.

Sciatic Nerve Function Evaluation: The rats were allowed to walk on white paper and leave their footprints every two weeks. The sciatic functional index (SFI) was calculated using the Bain-Mackinnon formula [45]:

$SFI = 109.5 \times \frac{E\times TS - N\times TS}{N} \times TS - 38.3 \times \frac{E\times PL - N\times PL}{N} \times PL + 13.3 \times \frac{E\times IT - N\times IT}{N} \times IT - 8.8$ where E and N denote experimental (operated) and normal (contralateral) sides, respectively, for toe spread (TS), print length (PL), and intermediate toe spread (IT). SFI = 0 indicates normal function, while SFI = −100 represents complete dysfunction [45]. Three blinded examiners performed all measurements.

Electromyography (EMG) Signal Recording: EMG signals were acquired from the gastrocnemius muscle using a Biopac MP36 instrument (Biopac Systems, Inc., CA, USA) equipped with a concentric needle electrode while applying a voltage of 1.5 V to the sciatic nerve for stimulation with a plexiglas-platinum electrode.

2.5.2. Nerve regeneration histological analysis

Following electrophysiological assessments, a 10 mm segment of the regenerated right sciatic nerve was dissected, and the nerve guidance conduit (NGC) was carefully removed, preserving the regenerated nerve inside. The conduit was then opened to expose the nerve. Some nerve samples were sectioned into 5 μm ultrathin slices for histological evaluation with 1 % toluidine blue staining and immunofluorescence staining with S100β (1:500, servicebio, Wuhan, China) and NF200 (1:500, servicebio, Wuhan, China), while others were prepared for ultrastructural analysis using transmission electron microscopy (TEM). Briefly, regenerated nerve samples were fixed in 2.5 % glutaraldehyde, dehydrated through graded ethanol, and embedded in EPON™ resin. Ultrathin sections (80 nm) were stained with uranyl acetate and lead citrate after ultramicrotomy. Images were captured using a TEM microscope (HT7700, Hitachi High-Tech, Tokyo, Japan) and stored for further analysis. The relative fluorescence intensity of S100β and NF200, the average diameters of myelinated fibers, and the myelin sheath thickness were quantified using Image J software.

2.5.3. *Gastrocnemius muscle evaluation*

The left and right gastrocnemius muscles were harvested at 6 and 12 weeks post-surgery and NGC implantation, rinsed with PBS, and weighed. The muscle weight ratio was calculated by comparing the operated-side (right) muscle weight with the non-operated (left) control.

For histological analysis, the muscles were fixed in 4 % paraformaldehyde overnight, paraffin-embedded, and sectioned into 4-μm slices using a microtome (RM2016, Leica, Germany). Masson's trichrome staining was performed per manufacturer's protocol. Collagen fiber percentage was calculated from ≥3 random fields using Image J software, with images captured on a Leica DM 6B optical microscope.

2.6. *Statistical analysis*

Results are presented as mean ± SD with biological replicates (n ≥ 3). Comparisons used one-way ANOVA with Tukey's post-hoc test or unpaired Student's t-tests (GraphPad Prism 10.1.2). Significance levels: *p < 0.05, **p < 0.01, ***p < 0.001, ****p < 0.0001.

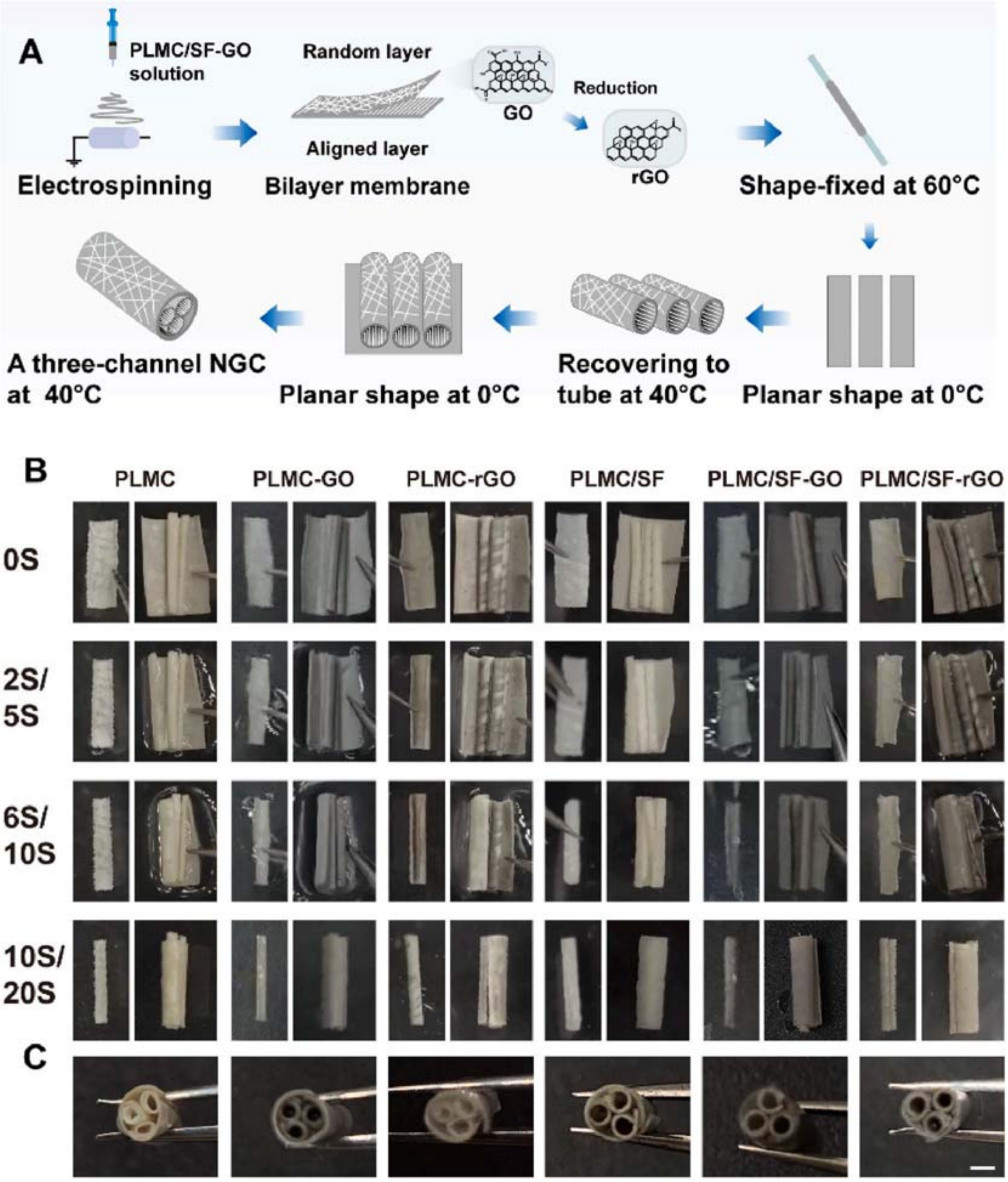

Fig. 3. Shape recovery properties of NGCs. (A) Schematic illustration of the fabrication of the three-channel NGC. (B) Shape recovery process of small and large tubes of PLMC, PLMC-GO, PLMC-rGO, PLMC/SF, PLMC/SF-GO and PLMC/SF-rGO conduits. Shape recovery for all conduits was achieved in warm water (40 °C) in less than 20 s, confirming the rapid response of the material. Scale bar: 1 mm. (C) Macromorphology of three different conduits. Scale bar: 1 cm.

3. Results and discussions

3.1. Fabrication and characterization of NGCs

By thermally programming temperature-responsive shape memory nanofiber membranes into a tubular shape at a high temperature, the membranes can unfold into a temporary flat shape in a 0 °C environment and subsequently recover to their original tubular shape at 40 °C (Fig. 3A). According to this method, a three-channel conduit was formed by combining one large tube (inner diameter 2 mm) with three smaller tubes (inner diameter 0.8 mm each), and the resulting tubular structure was stable at physiological temperatures. This three-channel conduit was prepared by electrospinning from random and oriented bilayer fiber membranes, with the outer layer of random fibers providing mechanical support for the conudit structure and triggering shape changes in response to temperature, while the inner layer of oriented nanofibers was used for directional guidance of cell growth [46]. Shape recovery from temporary planar to permanent tubular shape took 10 s for small tubes and 20 s for a large tube in 40 °C water (Fig. 3B). The deformation process is notably rapid (please see Video S1, Supporting Information). The multichannel conduit was rapidly fabricated by integrating three small tubes with one large tube, maintaining the tubular structure stable over a physiological temperature range below the Tg. Ultimately, PLMC, PLMC/GO, PLMC-rGO, PLMC/SF, PLMC/SF-GO and PLMC/SF-rGO three-channel nerve conduits were finally obtained (Fig. 3C). Crucially, this structure synergizes with thermo-responsive shape-memory properties to overcome a fundamental limitation of conventional fixed-size NGCs: dimensional mismatch. Our SMP-NGC addresses this by enabling programmable radial expansion via entropy-driven molecular chain reorganization. During the surgical procedure, following exposure of the nerve stumps at the defect site, the severed nerve ends will be positioned on the conduit membrane. Within 20 s following localized warming using a sterile warm saline rinse (40 °C), the membrane undergoes autonomous curling to circumferentially encapsulate the nerve, enabling tension-free coaptation with optimal anatomical alignment. This mechanism will significantly simplify the surgical technique while preventing iatrogenic trauma and ensuring a precise, tension-free fit across diverse defect sizes intraoperatively. This eliminates the need for extensive conduit inventories and mitigates complications related to size mismatch. Furthermore, this approach

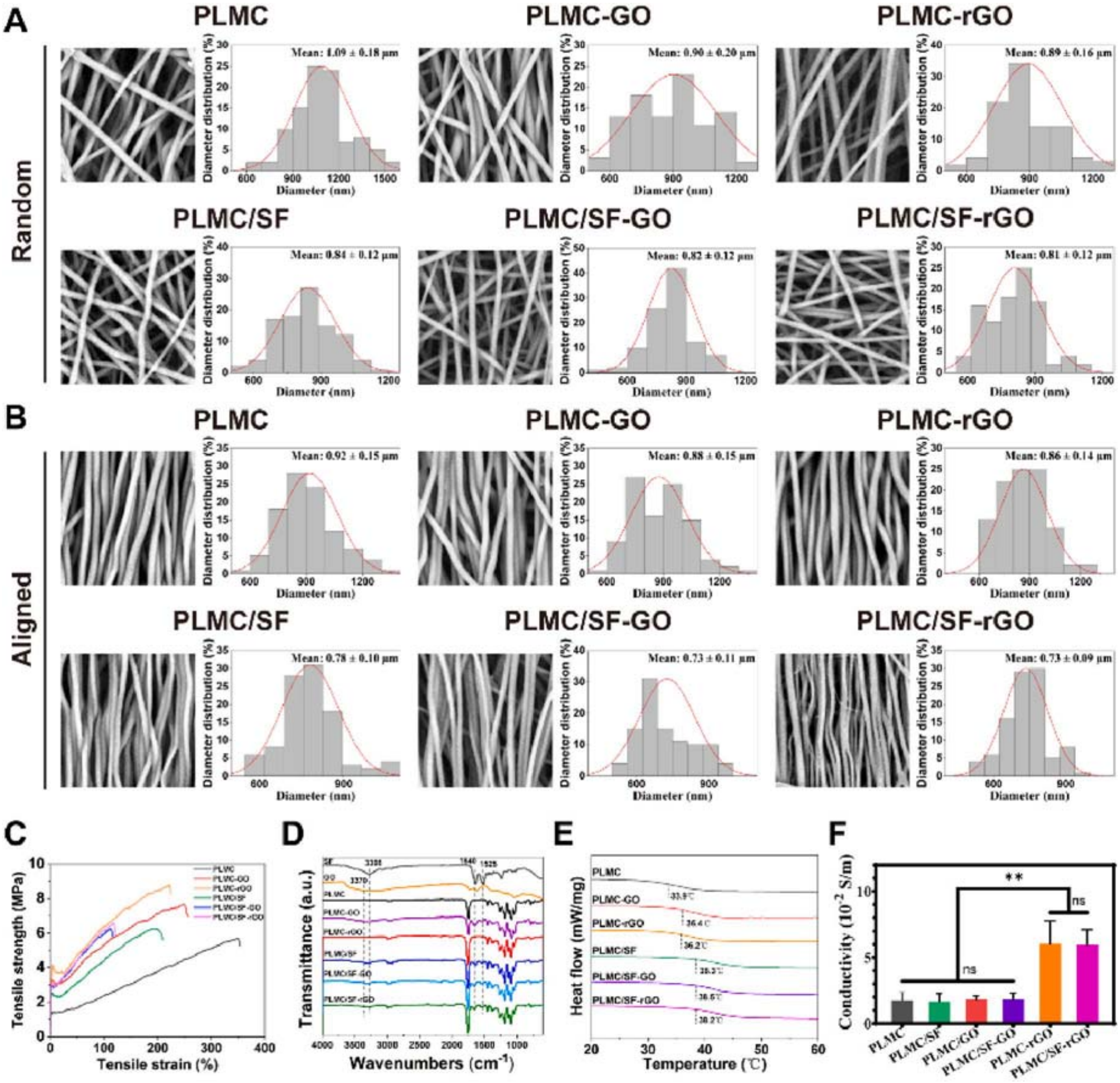

Fig. 4. Characterization of NGCs. (A) SEM images of random layers of PLMC, PLMC-GO, PLMC-rGO, PLMC/SF, PLMC/SF-GO, and PLMC/SF-rGO nanofiber membranes. (B) SEM images of aligned layers of these nanofibers. Scale bar: 5 μm. (C) Stress-strain curves of these different membranes. (D) FTIR spectra of different membranes. (E) DSC curves of different membranes. (F) The electrical conductivity of membranes. (n = 3).

offers significant practical advantages over 3D-printed NGCs. While 3D printing allows customization, it requires costly/preoperative steps: imaging, computational modeling, lengthy printing, and sterilization [47–49].

When observed under SEM, electrospun membranes with an outer layer of random nanofibers and an inner layer of aligned nanofibers were smooth and bead-less observed (Fig. 4A and B). As shown in Fig. 4A, the PLMC random nanofibers exhibited the largest average diameter with an average of 1.09 ± 0.18 μm. With the addition of GO and reduced, the average diameters of nanofiber membranes decreased to 0.89 ± 0.16 μm for PLMC-rGO. The difference in diameter distribution is primarily attributed to the enhanced conductivity resulting from the addition of GO to the electrospun solution, which pulls the nanofiber to a smaller average diameter under the identical electric field. At the same time, the average diameters of PLMC/SF (0.84 ± 0.12 μm) were smaller than that of PLMC nanofibers due to the addition of SF, which was consistent with previous research [50,51]. In the PLMC/SF-rGO nanofibers, the presence of GO further reduced the fiber diameters to 0.81 ± 0.12 μm. The statistical results of the nanofiber diameters in the aligned layer showed a consistent trend with those in the random layer (Fig. 4B). Moreover, the nanofibers of PLMC-rGO and PLMC/SF-rGO maintained a clear structure, indicating that the reduction of GO using L-ascorbic acid did not alter their morphology.

The autologously transplanted sciatic nerves showed a maximum stress of 1930 ± 50 kPa and a strain of 18.00 ± 1.30 % as reported [52]. The stress-strain curves indicated that the maximum stress and strain of materials meet the essential mechanical thresholds for neural conduits (Fig. 4C). The FTIR spectra demonstrated that the peaks at 3308 cm^{-1}, 1640 cm^{-1} and 1520 cm^{-1} were attributed to free amino and hydroxyl groups, amide I, and amide II of SF, respectively [53]. These peaks were observed in PLMC/SF and PLMC/SF-rGO nanofiber membranes (Fig. 4D). Additionally, the intensity of the hydroxyl group telescopic vibration peak of GO at 3370 cm^{-1} showed a significant attenuation after the reduction of GO in PLMC-rGO and PLMC/SF-rGO compared to GO [54]. These findings confirmed the successful incorporation of SF and rGO into nanofibers. As illustrated in Fig. 4E, the glass transition temperatures (Tg) of the PLMC, PLMC-rGO, PLMC/SF, and PLMC/SF-rGO membranes were measured at 33.9 °C, 36.2 °C, 38.3 °C, and 38.2 °C, respectively. To ensure the shape memory process was fully completed, a temperature exceeding the Tg was necessary [43]. Therefore, 40 °C was selected as the deformation temperature. To quantify the effect of rGO addition on the electrical conductivity of membranes, the conductivity was tested. The results showed that the electrical conductivity of PLMC, PLMC-GO, PLMC/SF, PLMC/SF-GO, PLMC-rGO, and PLMC/SF-rGO membranes was $1.75 \pm 0.61 \times 10^{-2}$ S m^{-1}, $1.84 \pm 0.24 \times 10^{-2}$ S m^{-1}, $1.67 \pm 0.59 \times 10^{-2}$ S, $1.83 \pm 0.47 \times 10^{-2}$ S m^{-1}, $6.02 \pm 1.77 \times 10^{-2}$ S m^{-1}, $5.97 \pm 1.15 \times 10^{-2}$ S m^{-1}, respectively. Notably, the electrical conductivity of PLMC-rGO and PLMC/SF-rGO scaffolds was significantly higher than that of other scaffolds (Fig. 4F), which is attributed to the restored electrical conductivity of rGO [39]. All NGCs demonstrated a slow degradation rate and desirable biodegradability in vitro. Notably, their multichannel structure was preserved with no signs of collapse after 30 days of immersion (Fig. S1).

3.2. Cell viability, proliferation, differentiation, adhesion and migration on PLMC/SF-rGO nanofiber membrane

Notably, a lot of studies on the safety concerns of GO, rGO and their derivatives showed a dose-dependent cytotoxicity [55–57]. CCK-8 assay identified 0.5 % rGO as the optimal concentration within PLMC/SF nanofiber membranes for RSC96 proliferation. While PLMC/SF-0.25 % rGO and PLMC/SF-0.5 %rGO significantly enhanced proliferation compared to PLMC/SF at 24 h ($p < 0.05$), higher rGO concentrations (1 %, 2 %) significantly inhibited proliferation ($p < 0.05$) (Fig. 5A). This indicated that rGO was relatively biocompatible at a low level, though overdose of rGO in the PLMC/SF scaffolds would eliminate the cell proliferation, which is consistent with previous studies [58]. The optimal amount of rGO in the PLMC/SF scaffold would promote the greatest extent of RSC proliferation, which is important for further evaluating cell attachment, viability, and neural expression. Under consideration of the greatest biocompatibility, the PLMC/SF -0.5 % rGO scaffold was selected for further evaluation.

LIVE/DEAD staining further revealed significantly higher cell viability on PLMC/SF and PLMC/SF-0.5 %rGO nanofiber membranes compared to PLMC and PLMC-rGO for both RSC96 and PC12 cells after 24 h (Fig. 5B and C). These results indicated that the incorporation of SF significantly improved the biocompatibility of nanofibrous scaffolds, which was consistent with previous studies. Long-term proliferation (7 days) was significantly enhanced on PLMC/SF and PLMC/SF-0.5 %rGO nanofiber membranes compared to PLMC for both cell types (Fig. 5D and E). In conclusion, PLMC/SF-0.5 %rGO nanoscaffolds, this cell-friendly material, was found to be the most effective for cell proliferation, especially for PC12 cells.

F-actin staining demonstrated that aligned nanofibers effectively guided cellular orientation, with RSC96 and PC12 cells exhibiting preferential alignment angles between 0° and 30° relative to the fiber direction on all nanofiber membranes (Fig. 5F and G). Thus, the aligned nanofibers fabricated by electrospinning technique can effectively guide the neurite growth, which is consistent with previous finding [59]. F-actin plays a pivotal role in neural development and repair, critically regulating adhesion, migration, and differentiation processes in both neuronal and glial cells. PLMC/SF-0.5 %rGO induced the highest F-actin expression intensity in both cell types (Fig. 5H). PC12 cells cultured on PLMC/SF-0.5 %rGO exhibited superior differentiation, characterized by a significantly higher percentage of differentiated cells and longer neurites compared to other nanofiber membranes (Fig. 5I and J). Thess enhancements is likely attributed to the restored electrical conductivity of rGO [39,60,61], and residual oxygen-containing functional groups improving surface hydrophilicity and bioactivity [37]. The markedly higher cell viability, F-actin expression—indicative of cytoskeletal organization and cellular maturation—as well as enhanced PC12 differentiation and neurite outgrowth observed on PLMC/SF-0.5 %rGO nanofiber membranes underscore the synergistic effects arising from the integration of the diverse amino acid residues in SF [62] with the electrical conductivity of rGO. Furthermore, the aligned nanofiber topography effectively guided cellular orientation, a critical factor for directed axonal regrowth. The enhanced Schwann cell migration observed on PLMC/SF-rGO nanofiber membranes, crucial for promoting axonal elongation and remyelination, highlights the favorable biointerface created by this composite material.

SEM confirmed robust cell adhesion on all nanofiber membranes, with RSC96 and PC12 cells extending neurites and surface protrusions. PLMC/SF-0.5 %rGO nanofiber membranes supported the highest cellular density and exhibited the most complex filopodial networks (Fig. 6A). Transwell and scratch assays demonstrated that PLMC/SF-0.5 %rGO nanofiber membranes significantly enhanced RSC96 migration compared to other groups (Fig. 6B–E). These findings demonstrated that the incorporation of rGO enhanced the potential of PLMC/SF nanoscaffolds in cellular adhesion and migration, which is vital in restoration after peripheral nerve injury (PNI).

3.3. Effects of multifunctional PLMC/SF-rGO NGCs on sciatic nerve regeneration

To investigate the in vivo effect of PLMC/SF-rGO NGCs in promoting nerve regeneration, we further included a long-term rat sciatic nerve defect model in this study. All the animals recovered without infection, edema, ulcers, or wound dehiscence. Conduits remained structurally intact at 12 weeks.

Functional recovery, assessed by SFI, was significantly improved in the PLMC/SF-rGO group compared to the PLMC/SF group at both 6 weeks (PLMC/SF-rGO: 67.4 ± 6.4; PLMC/SF: 79.8 ± 4.5; *$p < 0.05$) and

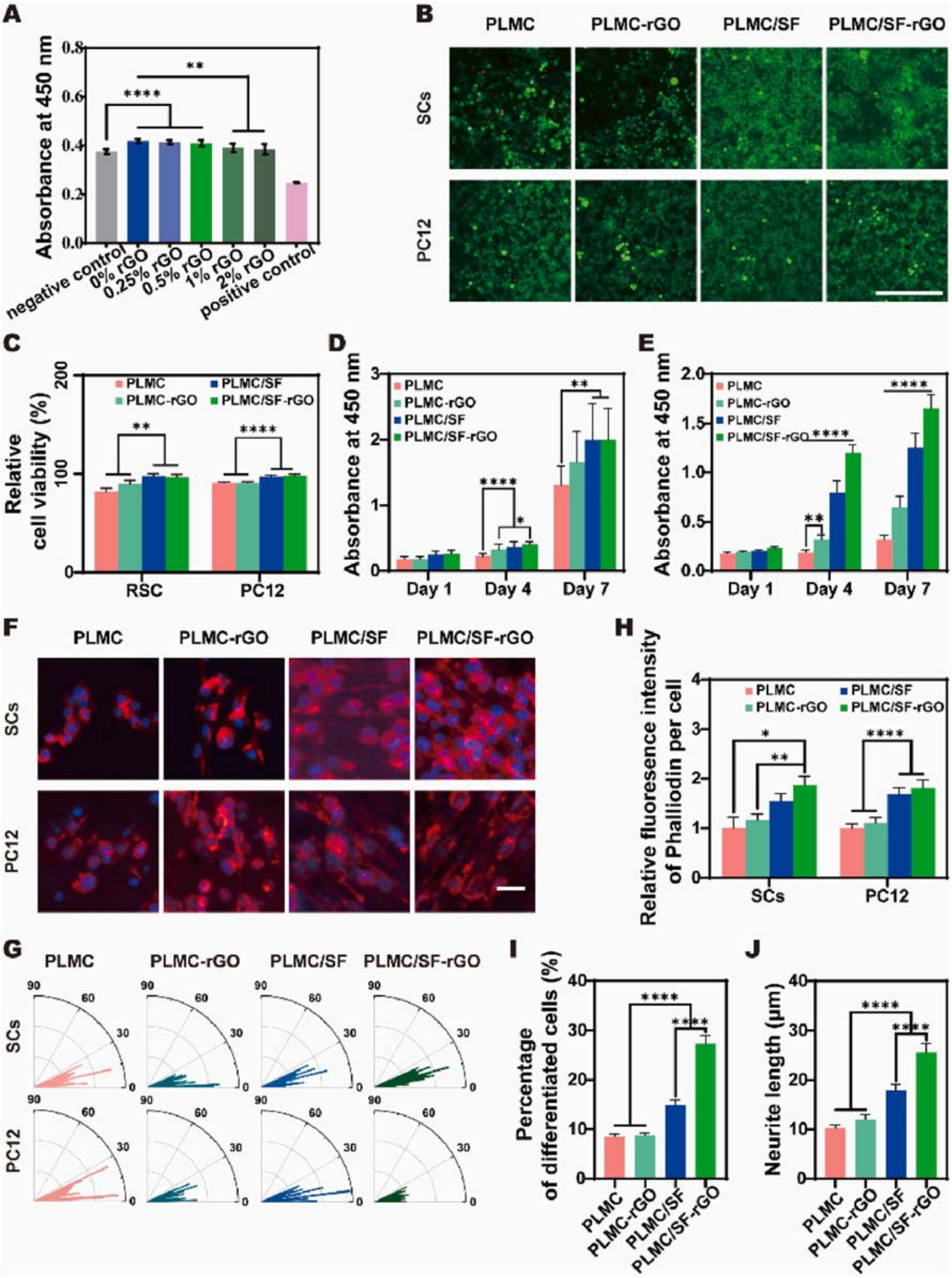

Fig. 5. Cell viability, proliferation, adhesion and differentiation on nanoscaffolds. (A) CCK-8 assay for RSCs cultured on PLMC/SF scaffolds with different concentrations of rGO, negative and positive control for 24 h (n = 6). (B) Live/dead staining of RSCs and PC12 cells on PLMC, PLMC-rGO, PLMC/SF and PLMC/SF-0.5 % rGO nanoscaffolds. Scale bar: 500 μm. (C) Cell viability as assayed by LIVE/DEAD cell staining in (B). (n = 5). (D) Cell proliferation for RSCs and (E) PC12 cells cultured on various nerve nanoscaffolds. (n = 10). (F) Phalloidin staining of RSCs and PC12 cells cultured on various nerve nanoscaffolds for 4 days. Scale bar: 50 μm. (G) Polar histograms of cellular growth on various nanoscaffolds. (H) Relative immunofluorescence intensity of phalloidin per cell in (F). (n = 5). (I) Differentiated cells and (J) neurite length of PC12 cells based on immunofluorescence images. (n = 5).

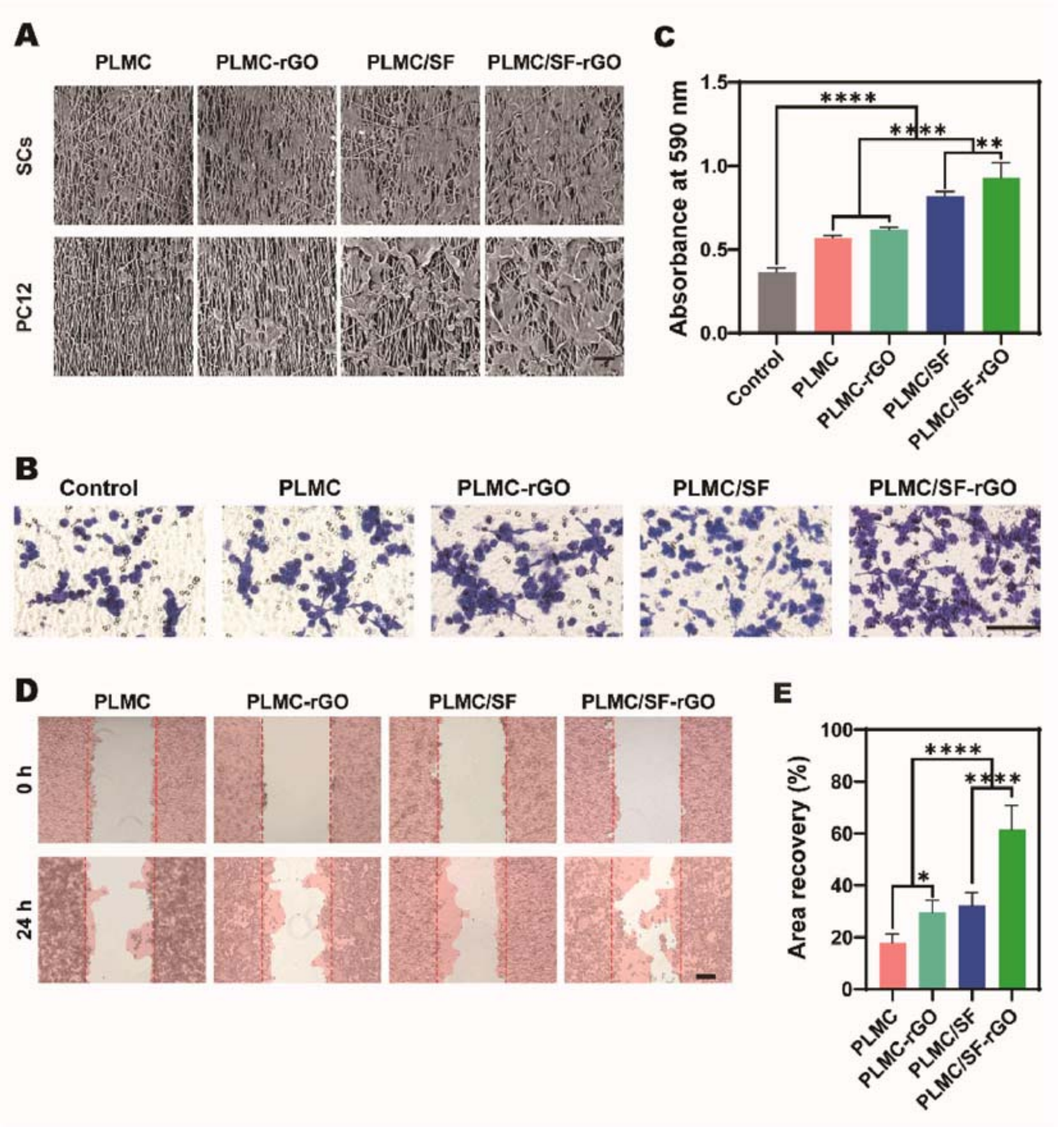

Fig. 6. Cell adhesion and migration on nerve nanoscaffolds. (A) SEM images of PC12 cells co-cultured on various nerve nanoscaffolds. Scale bar: 20 μm. (B) Images of migrated RSCs on substrates of different nanoscaffolds. Cells were stained purple with crystal violet. Scale bar: 100 μm. (C) Calculation of migration rate of RSCs. (n = 6). (D) Scratch test for RSCs on PLMC, PLMC-rGO, PLMC/SF and PLMC/SF-0.5 %rGO nanoscaffolds for 0 and 24 h. Scale bar: 200 μm. (E) Quantitative analysis of scratch test healing. (n = 5). (For interpretation of the references to colour in this figure legend, the reader is referred to the Web version of this article.)

12 weeks (PLMC/SF-rGO: 36.5 ± 3.1; PLMC/SF: 53.7 ± 5.4; $^*p < 0.05$). SFI values in the PLMC/SF-rGO group were comparable to the autograft group (6w: 63.8 ± 6.5, $p > 0.05$; 12w: 33.0 ± 2.8, $p > 0.05$) (Fig. 7B and C).

EMG analysis revealed similar nerve conduction velocities across groups at 6 and 12 weeks, confirming successful reinnervation. The PLMC/SF-rGO group exhibited significantly higher signal amplitudes than the PLMC/SF group at both timepoints (6w: 0.35 ± 0.04 mV vs. 0.27 ± 0.04 mV, $^*p < 0.05$; 12w: 0.51 ± 0.05 mV vs. 0.40 ± 0.04 mV, $^*p < 0.05$), approaching autograft levels (6w: 0.40 ± 0.05 mV; 12w: 0.57 ± 0.06 mV, $p > 0.05$) (Fig. 7D–F).

Incomplete nerve regeneration leads to muscle atrophy, which is characterized by a significant reduction in muscle mass and connective tissue hyperplasia. Muscle atrophy assessment showed significantly higher gastrocnemius muscle weight ratios in the PLMC/SF-rGO group compared to PLMC/SF at 6 weeks (59.0 ± 4.1 % vs. 49.2 ± 3.2 %, $^*p < 0.05$) and 12 weeks (79.6 ± 7.6 % vs. 67.0 ± 6.0 %, $^*p < 0.05$), comparable to autografts (6w: 63.0 ± 5.8 %; 12w: 85.0 ± 7.9 %, $p > 0.05$) (Fig. 7G). Apart from the loss of muscle tissue, denervation after nerve injury typically leads to pathological muscle remodeling-accumulation of fibrotic collagen within the muscle. Following successful neuromuscular reinnervation, gastrocnemius muscle exhibits progressive resolution of fibrotic remodeling. Masson's trichrome staining confirmed significantly reduced fibrotic collagen deposition in the PLMC/SF-rGO group compared to PLMC/SF at both 6 weeks (12.5 ± 1.4 % vs. 25.5 ± 2.3 %, $^*p < 0.05$) and 12 weeks (8.5 ± 0.9 % vs. 15.5 ± 1.6 %, $^*p < 0.05$), though still higher than autografts (6w: 7.1 ± 0.7 %; 12w: 1.5 ± 0.2 %) (Fig. 7H and I).

3.4. Histological evaluation of nerve regeneration

The structural repair of nerve tissues was examined through histological evaluation. During remyelination, which is a critical regeneration process for proper signal conduction in the peripheral nervous system, Schwann cells produce new myelin sheaths around regenerating axons. Appropriate regeneration is recognized by an increase in myelin sheath thickness and axon size. Toluidine blue staining and TEM revealed superior nerve regeneration in autograft and PLMC/SF-rGO

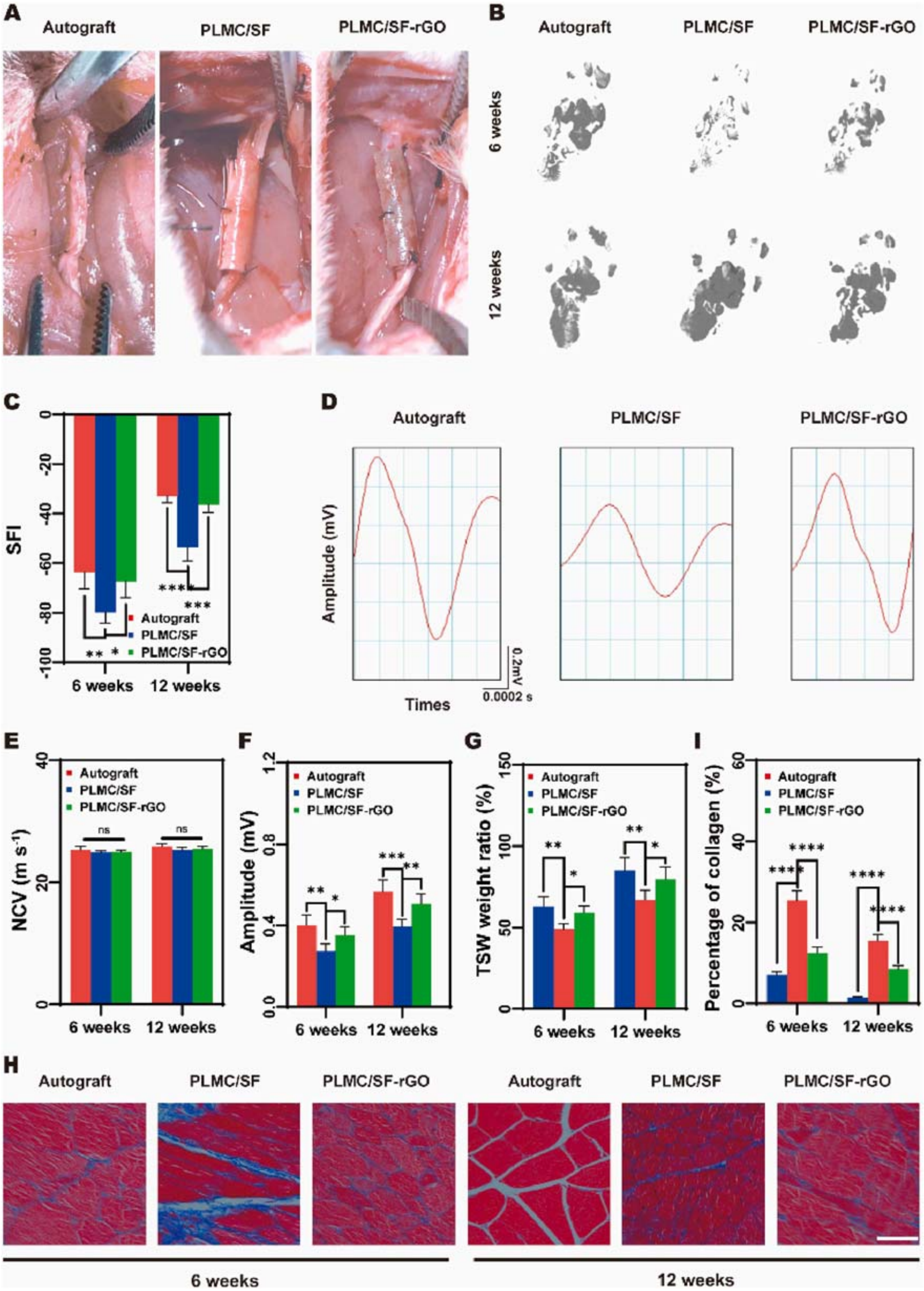

Fig. 7. In vivo NGC implantation and functional recovery. (A) Photographs of autograft and NGCs implantation. (B) Rat footprint map at 6 and 12 weeks. (C) Sciatic functional indices (SFIs) at 6 and 12 weeks. (n = 5). (D) EMG signals obtained at 12 weeks. (E) Nerve conduction velocity (NCV) at 6 and 12 weeks. (n = 5). (F) Onset-to-peak amplitudes at 6 and 12 weeks (n = 5). (G) TSW muscle wet weight ratios at 6 and 12 weeks. (n = 5). (H) Masson's trichrome staining of gastrocnemius muscles at 6 and 12 weeks. Scale bar: 50 μm. (I) Percentage of collagen in (H). (n = 5).

groups. Regenerated nerves in these groups displayed well-defined, thick, dense myelin sheaths and larger axon diameters, contrasting with the thin, loosely organized myelin observed in the PLMC/SF group (Fig. 8A and B). Quantitatively, PLMC/SF-rGO conduits supported significantly greater myelin sheath thickness (6w: 333 ± 41 nm; 12w: 592 ± 49 nm) and axon diameter (6w: 2.18 ± 0.16 μm; 12w: 3.60 ± 0.32 μm) compared to PLMC/SF conduits (Thickness: 6w: 210 ± 26 nm, 12w: 364 ± 30 nm; Diameter: 6w: 1.73 ± 0.14 μm, 12w: 2.50 ± 0.31 μm) at both timepoints (*$p < 0.05$), approaching autograft levels (Thickness: 6w: 379 ± 48 nm, 12w: 620 ± 57 nm; Diameter: 6w: 2.46 ± 0.25 μm, 12w: 3.96 ± 0.30 μm) (Fig. 8C and D).

Immunofluorescence staining (12 weeks) confirmed expression of axonal marker NF200 and Schwann cell marker S100β in all groups, indicating axonal regeneration and remyelination. Autografts exhibited the highest fluorescence intensity for both markers. Between conduit groups, PLMC/SF-rGO conduits demonstrated significantly higher NF200 and S100β expression compared to PLMC/SF conduits (*$p < 0.05$) (Fig. 8E–G), indicating enhanced axonal density and Schwann cell activity facilitated by rGO incorporation.

Overall, we successfully demonstrated that the PLMC/SF-based rGO NGC facilitated axon regrowth, myelination, and nerve regeneration, enabling the functional recovery of the injured peripheral nervous system.

4. Conclusion

In conclusion, we have fabricated a novel PLMC/SF-rGO NGC with structural and physical adaptivity that effectively addresses key limitations of current NGCs. Its biocompatibility, ability to promote Schwann cell and neuronal activities in vitro, and capacity to significantly accelerate structural and functional nerve regeneration in vivo to levels approaching autografts, position this novel conduit as a highly promising alternative for the clinical repair of critical-length peripheral nerve injuries. Future studies should focus on long-term biocompatibility, degradation profiles, and potential for further functionalization (e.g., growth factor delivery) to optimize outcomes in larger animal models. Our conduit system establishes a practical framework for personalized, scar-minimized peripheral nerve repair.

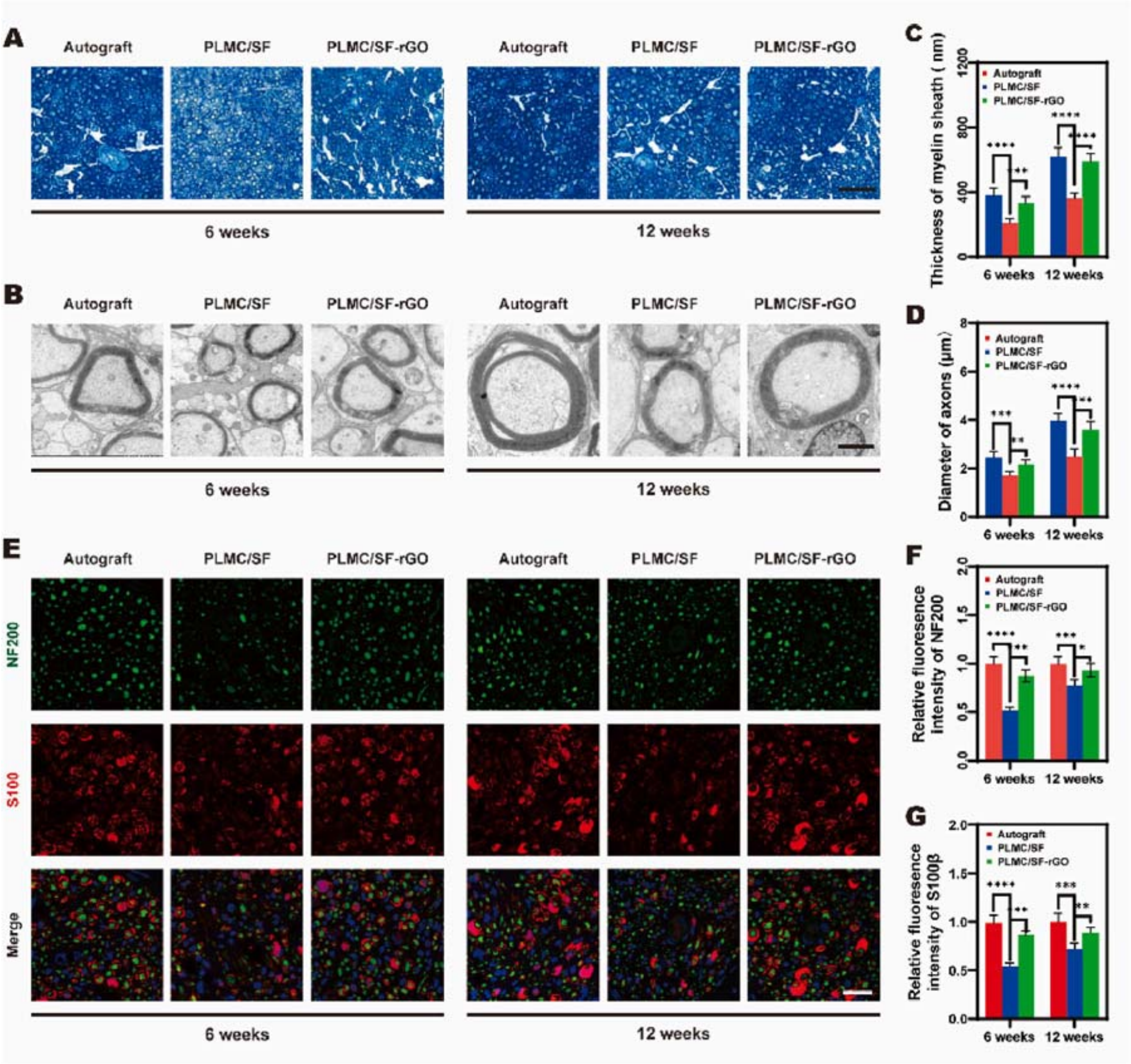

Fig. 8. Histological investigation of nerve regeneration. (A) Toluidine blue staining of regenerated sciatic nerves at 6 and 12 weeks. Scale bar: 50 μm. (B) Cross-sectional TEM images of the distal parts of regenerated nerves at 4000 magnifications. Scale bar: 2 μm. (C) Thickness of myelin sheath in regenerated sciatic nerve at 6 and 12 weeks analyzed from TEM images (n = 5). (D) Diameter of axons in regenerated sciatic nerves at 6 and 12 weeks analyzed from TEM images. (n = 5). (E) Immunofluorescence staining of S-100β (red), NF-200 (green), and nuclei (blue) at 6- and 12-weeks post-transplantation. Scale bar: 20 μm. (F) Relative fluorescence intensity of NF-200. (n = 5). (G) Relative fluorescence intensity of S-100β. (n = 5). (For interpretation of the references to colour in this figure legend, the reader is referred to the Web version of this article.)

CRediT authorship contribution statement

Tao Gao: Writing – original draft, Validation, Software, Methodology, Investigation, Data curation, Conceptualization. **Jiahui Song:** Writing – original draft, Software, Methodology, Investigation, Data curation. **Lu Li:** Writing – original draft, Software, Methodology, Investigation. **Junqing Lin:** Visualization, Software, Methodology, Investigation. **Junjie Shen:** Software, Methodology, Investigation. **Yun Qian:** Writing – review & editing, Supervision, Resources, Project administration, Funding acquisition, Conceptualization. **Xiumei Mo:** Writing – review & editing, Supervision, Resources, Project administration, Conceptualization. **Xianyou Zheng:** Writing – review & editing, Supervision, Resources, Project administration, Funding acquisition, Conceptualization.

Declaration of competing interest

The authors declare that they have no known competing financial interests or personal relationships that could have appeared to influence the work reported in this paper.

Acknowledgments

This work was supported in part by the Clinical Research Plan of SHDC (SHDC2023CRT011); Excellent Youth Cultivation Program of Shanghai Sixth People's Hospital (No. ynyq202201); Sino-German Mobility Programme (Grant No. M−0699); the Foundation of National Center for Translational Medicine (Shanghai) SHU Branch (No. SUITM-2025010); Laboratory Open Fund of Key Technology and Materials in Minimally Invasive Spine Surgery (2024JZWC-ZDA05); Shanghai Outstanding Academic Leader Plan (23XD1403000).

Appendix A. Supplementary data

Supplementary data to this article can be found online at https://doi.org/10.1016/j.mtbio.2025.102508.

Data availability

Data will be made available on request.

References

[1] B. Lopes, P. Sousa, R. Alvites, M. Branquinho, A.C. Sousa, C. Mendonça, L. M. Atayde, A.L. Luís, A.S.P. Varejão, A.C. Maurício, Peripheral nerve injury treatments and advances: one health perspective, Int. J. Mol. Sci. 23 (2) (2022).

[2] D. Grinsell, C.P. Keating, Peripheral nerve reconstruction after injury: a review of clinical and experimental therapies, BioMed Res. Int. 2014 (2014) 698256.

[3] J. Scheib, A. Höke, Advances in peripheral nerve regeneration, Nat. Rev. Neurol. 9 (12) (2013) 668–676.

[4] X. Wang, Y. Lei, K. Jiang, C. Yan, J. Shen, W. Zhao, C. Xiang, Z. Cai, Y. Song, L. Chen, W. Cui, Y. Li, Mito-battery: micro-nanohydrogel microspheres for targeted regulation of cellular mitochondrial respiratory chain, Nano Today 49 (2023) 101820.

[5] J. Lans, K.R. Eberlin, P.J. Evans, D. Mercer, J.A. Greenberg, J.F. Styron, A systematic review and meta-analysis of nerve gap repair: comparative effectiveness of allografts, autografts, and conduits, Plast. Reconstr. Surg. 151 (5) (2023) 814e–827e.

[6] N.G. Simon, R.J. Spinner, D.G. Kline, M. Kliot, Advances in the neurological and neurosurgical management of peripheral nerve trauma, J. Neurol. Neurosurg. Psychiatry 87 (2) (2016) 198–208.

[7] Y.K. Huang, Y.G. Lu, X. Zhao, J.B. Zhang, F.M. Zhang, Y. Chen, L.B. Bi, J.H. Gu, Z. J. Jiang, X.M. Wu, Q.Y. Li, Y. Liu, J.X. Shen, X.J. Liu, Cytokine activin C ameliorates chronic neuropathic pain in peripheral nerve injury rodents by modulating the TRPV1 channel, Br. J. Pharmacol. 177 (24) (2020) 5642–5657.

[8] Y. Liu, F. Kano, N. Hashimoto, L. Xia, Q. Zhou, X. Feng, H. Hibi, A. Miyazaki, T. Iwamoto, Y. Matsuka, Z. Zhang, E. Tanaka, A. Yamamoto, Conditioned medium from the stem cells of human exfoliated deciduous teeth ameliorates neuropathic pain in a partial sciatic nerve ligation model, Front. Pharmacol. 13 (2022) 745020.

[9] L. Zhao, C. Jiang, B. Yu, J. Zhu, Y. Sun, S. Yi, Single-cell profiling of cellular changes in the somatic peripheral nerves following nerve injury, Front. Pharmacol. 15 (2024) 1448253.

[10] D. Gu, Y. Xia, Z. Ding, J. Qian, X. Gu, H. Bai, M. Jiang, D. Yao, Inflammation in the peripheral nervous system after injury, Biomedicines 12 (6) (2024).

[11] Y. Yang, H.Y. Xu, Q.W. Deng, G.H. Wu, X. Zeng, H. Jin, L.J. Wang, B.Q. Lai, G. Li, Y.H. Ma, B. Jiang, J.W. Ruan, Y.Q. Wang, Y. Ding, Y.S. Zeng, Electroacupuncture facilitates the integration of a grafted TrkC-modified mesenchymal stem cell-derived neural network into transected spinal cord in rats via increasing neurotrophin-3, CNS Neurosci. Ther. 27 (7) (2021) 776–791.

[12] W. Zhou, M.S.U. Rahman, C. Sun, S. Li, N. Zhang, H. Chen, C.C. Han, S. Xu, Y. Liu, Perspectives on the novel multifunctional nerve guidance conduits: from specific regenerative procedures to motor function rebuilding, Adv. Mater. 36 (14) (2024) e2307805.

[13] J. Fang, L. Nan, K. Song, Z. Weng, J. Shan, V. Shahin, J. Liu, Y. Qian, Application and progress of bionic scaffolds in nerve repair: a narrative review, Adv. Technol. Neurosci. 1 (1) (2024) 43–50.

[14] M. Li, J. Zhou, Y. Ning, Y. Xiong, Chemical materials involved in neural tissue engineering scaffold techniques: a narrative review, Adv. Technol. Neurosci. 1 (2) (2024) 244–260.

[15] J. Zhang, Z. Liu, J. Wang, Y. Zhang, J. Dong, J. Gao, L. Zhang, J. Wang, P. Tang, Q. Zhang, 3D coaxially printing rGO aerogel-based biocompatible fiber for peripheral nerve regeneration, Adv. Fiber Mater. 6 (3) (2024) 713–726.

[16] Y. Liu, Q. Guo, X. Zhang, Y. Wang, X. Mo, T. Wu, Progress in electrospun fibers for manipulating cell behaviors, Adv. Fiber Mater. 5 (4) (2023) 1241–1272.

[17] Y. Wang, X. Zhang, L. Yao, Y. Yan, Y. Wang, T. Wu, "Cell climbing stones" – varying the surfaces of electrospun nanofibers with protrusions as secondary structures to manipulate neural cell behaviors, Nanoscale Horiz. 10 (10) (2025) 2411–2421.

[18] S. Kehoe, X.F. Zhang, D. Boyd, FDA approved guidance conduits and wraps for peripheral nerve injury: a review of materials and efficacy, Injury 43 (5) (2012) 553–572.

[19] W. Daly, L. Yao, D. Zeugolis, A. Windebank, A. Pandit, A biomaterials approach to peripheral nerve regeneration: bridging the peripheral nerve gap and enhancing functional recovery, J. R. Soc., Interface 9 (67) (2012) 202–221.

[20] S. Yan, F. Zhang, L. Luo, L. Wang, Y. Liu, J. Leng, Shape memory polymer composites: 4D printing, Smart Struct. Appl. 6 (2023) 234. Research (Wash D C).

[21] Liu, Emerging trends in injectable stimuliâ€\x90ronsive Hydhogel Micmospheres: Desdgn Strstegies and Thetapeutic Innivations, Medcomm - Biomater. Appl. 4 (2) (2025).

[22] H.M. Khan, X. Liao, B.A. Sheikh, Y. Wang, Z. Su, C. Guo, Z. Li, C. Zhou, Y. Cen, Q. Kong, Smart biomaterials and their potential applications in tissue engineering, J. Mater. Chem. B 10 (36) (2022) 6859–6895.

[23] H. Bao, Y. Tian, H. Wang, T. Ye, S. Wang, J. Zhao, Y. Qiu, J. Li, C. Pan, G. Ma, W. Wei, Y. Tao, Exosome-loaded degradable polymeric microcapsules for the treatment of vitreoretinal diseases, Nat. Biomed. Eng. 8 (11) (2024) 1436–1452.

[24] C. Li, W. Zhang, Y. Nie, X. Du, C. Huang, L. Li, J. Long, X. Wang, W. Tong, L. Qin, Y. Lai, Time-sequential and multi-functional 3d printed Mgo2/PLGA scaffold developed as A novel biodegradable and bioactive bone substitute for challenging postsurgical osteosarcoma treatment, Adv. Mater. (2023) e2308875.

[25] J. He, X. Hu, J. Cao, Y. Zhang, J. Xiao, L. Peng, D. Chen, C. Xiong, L. Zhang, Chitosan-coated hydroxyapatite and drug-loaded polytrimethylene carbonate/polylactic acid scaffold for enhancing bone regeneration, Carbohydr. Polym. 253 (2021) 117198.

[26] H. Zhang, L. Sun, J. Guo, Y. Zhao, Hierarchical spinning of Janus Textiles with anisotropic wettability for wound healing, Research 6 (2023) 129.

[27] S. Choudhury, A. Joshi, A. Agrawal, A. Nain, A. Bagde, A. Patel, Z.Q. Syed, S. Asthana, K. Chatterjee, NIR-responsive deployable and self-fitting 4D-Printed bone tissue scaffold, ACS Appl. Mater. Interfaces (2024).

[28] S. Choudhury, A. Joshi, V.S. Baghel, G.K. Ananthasuresh, S. Asthana, S. Homer-Vanniasinkam, K. Chatterjee, Design-encoded dual shape-morphing and shape-memory in 4D printed polymer parts toward cellularized vascular grafts, J. Mater. Chem. B (2024).

[29] J. Song, J. Dong, Z. Yuan, M. Huang, X. Yu, Y. Zhao, Y. Shen, J. Wu, M. El-Newehy, M.M. Abdulhameed, B. Sun, J. Chen, X. Mo, Shape-persistent conductive nerve guidance conduits for peripheral nerve regeneration, Adv. Healthcare Mater. (2024) e2401160.

[30] J. Liu, C. Du, J. Chen, B. Tang, S. Liu, J. Tan, X. Luo, J. Zhan, J. Liu, Z. Chen, Y. Zhang, Z.A. Li, W. Huang, Y. Lei, Hydrogel microspheres empowering Organ-on-a-Chip systems: innovations and applications, Small(n/a) 2504563.

[31] Y. Zhang, R. Sheng, J. Chen, H. Wang, Y. Zhu, Z. Cao, X. Zhao, Z. Wang, C. Liu, Z. Chen, P. Zhang, B. Kuang, H. Zheng, C. Shen, Q. Yao, W. Zhang, Silk fibroin and sericin differentially potentiate the paracrine and regenerative functions of stem cells through multiomics analysis, Adv. Mater. 35 (20) (2023) e2210517.

[32] J. Shin, E.J. Choi, J.H. Cho, A.N. Cho, Y. Jin, K. Yang, C. Song, S.W. Cho, Three-dimensional electroconductive hyaluronic acid hydrogels incorporated with carbon nanotubes and polypyrrole by catechol-mediated dispersion enhance neurogenesis of human neural stem cells, Biomacromolecules 18 (10) (2017) 3060–3072.

[33] Y. Wu, D. Xiao, P. Liu, Q. Liao, Q. Ruan, C. Huang, L. Liu, D. Li, X. Zhang, W. Li, K. Tang, Z. Wu, G. Wang, H. Wang, P.K. Chu, Nanostructured conductive polypyrrole for antibacterial components in flexible wearable devices, Research 6 (2023) 74.

[34] J. Liu, C. Du, H. Chen, W. Huang, Y. Lei, Nano-micron combined hydrogel microspheres: novel answer for minimal invasive biomedical applications, Macromol. Rapid Commun. (2024) e2300670.

[35] A. Ambrosi, C.K. Chua, A. Bonanni, M. Pumera, Electrochemistry of graphene and related materials, Chem. Rev. 114 (14) (2014) 7150–7188.

[36] Y. Zhang, S.F. Ali, E. Dervishi, Y. Xu, Z. Li, D. Casciano, A.S. Biris, Cytotoxicity effects of graphene and single-wall carbon nanotubes in neural phaeochromocytoma-derived PC12 cells, ACS Nano 4 (6) (2010) 3181–3186.

[37] Y. Wang, B. Yang, Z. Huang, Z. Yang, J. Wang, Q. Ao, G. Yin, Y. Li, Progress and mechanism of graphene oxide-composited materials in application of peripheral nerve repair, Colloids Surf. B Biointerfaces 234 (2023) 113672.

[38] Y. Hui, Z. Yan, H. Yang, X. Xu, W.-E. Yuan, Y. Qian, Graphene family nanomaterials for stem cell neurogenic differentiation and peripheral nerve regeneration, ACS Appl. Bio Mater. 5 (10) (2022) 4741–4759.

[39] A. Magaz, X. Li, J.E. Gough, J.J. Blaker, Graphene oxide and electroactive reduced graphene oxide-based composite fibrous scaffolds for engineering excitable nerve tissue, Mater. Sci. Eng., C 119 (2021) 111632.

[40] L. Wang, C. Lu, S. Yang, P. Sun, Y. Wang, Y. Guan, S. Liu, D. Cheng, H. Meng, Q. Wang, J. He, H. Hou, H. Li, W. Lu, Y. Zhao, J. Wang, Y. Zhu, Y. Li, D. Luo, T. Li, H. Chen, S. Wang, X. Sheng, W. Xiong, X. Wang, J. Peng, L. Yin, A fully biodegradable and self-electrified device for neuroregenerative medicine, Sci. Adv. 6 (50) (2020).

[41] P.A. Wieringa, A.R. Gonçalves de Pinho, S. Micera, R.J.A. van Wezel, L. Moroni, Biomimetic architectures for peripheral nerve repair: a review of biofabrication strategies, Adv. Healthcare Mater. 7 (8) (2018) e1701164.

[42] N. Liu, X. Ning, X. Zhang, Z. Zhou, M. Fu, Y. Wang, T. Wu, Gradient galectin-1 coating technology: bionic multichannel nerve guidance conduits promote neural cell migration, Adv. Technol. Neurosci. 1 (2) (2024) 276–289.

[43] J. Wang, H. Xiong, T. Zhu, Y. Liu, H. Pan, C. Fan, X. Zhao, W.W. Lu, Bioinspired multichannel nerve guidance conduit based on shape memory nanofibers for potential application in peripheral nerve repair, ACS Nano 14 (10) (2020) 12579–12595.

[44] Y. Qian, J. Song, X. Zhao, W. Chen, Y. Ouyang, W. Yuan, C. Fan, 3D fabrication with integration molding of a graphene oxide/polycaprolactone nanoscaffold for neurite regeneration and angiogenesis, Adv. Sci. (Weinh.) 5 (4) (2018) 1700499.

[45] F. Kanaya, J.C. Firrell, W.C. Breidenbach, Sciatic function index, nerve conduction tests, muscle contraction, and axon morphometry as indicators of regeneration, Plast. Reconstr. Surg. 98 (7) (1996) 1264–1271, discussion 1272–4.

[46] G. Hong, Z. Hu, Y. Zhou, M. Chen, H. Wu, W. Lu, W. Jin, K. Yao, Z. Xie, J. Shi, An integrated dual-layer heterogeneous polycaprolactone scaffold promotes oral mucosal wound healing through inhibiting bacterial adhesion and mediating HGF-1 behavior, Research 7 (2024) 499.

[47] C.F. He, T.H. Qiao, X.C. Ren, M. Xie, Q. Gao, C.Q. Xie, P. Wang, Y. Sun, H. Yang, Y. He, Printability in multi-material projection-based 3-dimensional bioprinting, Research 8 (2025) 613.

[48] Y. Fang, C. Wang, Z. Liu, J. Ko, L. Chen, T. Zhang, Z. Xiong, L. Zhang, W. Sun, 3D printed conductive multiscale nerve guidance conduit with hierarchical fibers for peripheral nerve regeneration, Adv. Sci. (Weinh.) 10 (12) (2023) e2205744.

[49] C. Du, W. Huang, Y. Lei, The application and prospects of 3D printable microgel in biomedical science and engineering, Int. J. Bioprint 9 (5) (2023) 753.

[50] P. Gu, Y. Mao, W. Lu, W. Chen, Silk fibroin incorporated electrospun aliphatic polyester nanofiber scaffolds with excellent dimensional stability and cytocompatibility, Eur. Polym. J. 211 (2024) 113039.

[51] Y. Fang, Z. Liu, Y. Jin, Y. Huang, S. Zhou, H. Tian, H. Wu, Electrospun high hydrophilicity antimicrobial poly (lactic acid)/silk fibroin nanofiber membrane for wound dressings, Int. J. Biol. Macromol. (2024) 133905.

[52] Q. Dong, X. Yang, X. Liang, J. Liu, B. Wang, Y. Zhao, C. Huselstein, X. Feng, Z. Tong, Y. Chen, Composite hydrogel conduit incorporated with platelet-rich plasma improved the regenerative microenvironment for peripheral nerve repair, ACS Appl. Mater. Interfaces 15 (20) (2023) 24120–24133.

[53] L. Lins, R. Brasseur, The hydrophobic effect in protein folding, FASEB J. 9 (7) (1995) 535–540.

[54] J. Wang, Y. Cheng, L. Chen, T. Zhu, K. Ye, C. Jia, H. Wang, M. Zhu, C. Fan, X. Mo, In vitro and in vivo studies of electroactive reduced graphene oxide-modified nanofiber scaffolds for peripheral nerve regeneration, Acta Biomater. 84 (2019) 98–113.

[55] Y. Xiao, Y.X. Pang, Y. Yan, P. Qian, H. Zhao, S. Manickam, T. Wu, C.H. Pang, Synthesis and functionalization of graphene materials for biomedical applications: recent advances, challenges, and perspectives, Adv. Sci. (Weinh.) 10 (9) (2023) e2205292.

[56] T.A. Tabish, M.Z. Hussain, S. Zervou, W.K. Myers, W. Tu, J. Xu, I. Beer, W. E. Huang, R. Chandrawati, M.J. Crabtree, P.G. Winyard, C.A. Lygate, S-nitrosocysteamine-functionalised porous graphene oxide nanosheets as nitric oxide delivery vehicles for cardiovascular applications, Redox Biol. 72 (2024) 103144.

[57] Z.W. Yan, T.B. Ye, L. Yang, H.Q. Jiang, C. Chen, S.L. Chen, Y. Qian, C.Y. Fan, Nanobiology dependent therapeutic convergence between biocompatibility and bioeffectiveness of graphene oxide quantum dot scaffold for immuno-inductive angiogenesis and nerve regeneration, Adv. Funct. Mater. 33 (9) (2023).

[58] S. Kanakia, J.D. Toussaint, S. Mullick Chowdhury, T. Tembulkar, S. Lee, Y.P. Jiang, R.Z. Lin, K.R. Shroyer, W. Moore, B. Sitharaman, Dose ranging, expanded acute toxicity and safety pharmacology studies for intravenously administered functionalized graphene nanoparticle formulations, Biomaterials 35 (25) (2014) 7022–7031.

[59] T. Li, Q. Cheng, J. Zhang, B. Liu, Y. Shi, H. Wang, L. Huang, S. Zhang, R. Zhang, S. Wang, G. Lu, P. Tang, Z. Liu, K. Wang, A novel flexible nerve guidance conduit promotes nerve regeneration while providing excellent mechanical properties, Neur. Regen. Res. 20 (7) (2025) 2084–2094.

[60] X. Yao, Z. Yan, X. Wang, H. Jiang, Y. Qian, C. Fan, The influence of reduced graphene oxide on stem cells: a perspective in peripheral nerve regeneration, Regen. Biomater. 8 (4) (2021).

[61] M. Tang, Q. Song, N. Li, Z. Jiang, R. Huang, G. Cheng, Enhancement of electrical signaling in neural networks on graphene films, Biomaterials 34 (27) (2013) 6402–6411.

[62] Z. Mao, X. Bi, C. Yu, L. Chen, J. Shen, Y. Huang, Z. Wu, H. Qi, J. Guan, X. Shu, B. Yu, Y. Zheng, Mechanically robust and personalized silk fibroin-magnesium composite scaffolds with water-responsive shape-memory for irregular bone regeneration, Nat. Commun. 15 (1) (2024) 4160.